A stochastic extension of the explicit algebraic subgrid-scale models

A. Rasam, G. Brethouwer, and A. V. Johansson

Citation: Physics of Fluids (1994-present) **26**, 055113 (2014); doi: 10.1063/1.4879436
View online: http://dx.doi.org/10.1063/1.4879436
View Table of Contents: http://scitation.aip.org/content/aip/journal/pof2/26/5?ver=pdfcov
Published by the AIP Publishing

PHYSICS OF FLUIDS **26**, 055113 (2014)

A stochastic extension of the explicit algebraic subgrid-scale models

A. Rasam,[a] G. Brethouwer, and A. V. Johansson
Linné FLOW Centre, KTH Mechanics, SE-100 44 Stockholm, Sweden

(Received 12 November 2013; accepted 10 May 2014; published online 29 May 2014)

The explicit algebraic subgrid-scale (SGS) stress model (EASM) of Marstorp *et al.* ["Explicit algebraic subgrid stress models with application to rotating channel flow," J. Fluid Mech. **639**, 403–432 (2009)] and explicit algebraic SGS scalar flux model (EASFM) of Rasam *et al.* ["An explicit algebraic model for the subgrid-scale passive scalar flux," J. Fluid Mech. **721**, 541–577 (2013)] are extended with stochastic terms based on the Langevin equation formalism for the subgrid-scales by Marstorp *et al.* ["A stochastic subgrid model with application to turbulent flow and scalar mixing," Phys. Fluids **19**, 035107 (2007)]. The EASM and EASFM are nonlinear mixed and tensor eddy-diffusivity models, which improve large eddy simulation (LES) predictions of the mean flow, Reynolds stresses, and scalar fluxes of wall-bounded flows compared to isotropic eddy-viscosity and eddy-diffusivity SGS models, especially at coarse resolutions. The purpose of the stochastic extension of the explicit algebraic SGS models is to further improve the characteristics of the kinetic energy and scalar variance SGS dissipation, which are key quantities that govern the small-scale mixing and dispersion dynamics. LES of turbulent channel flow with passive scalar transport shows that the stochastic terms enhance SGS dissipation statistics such as length scale, variance, and probability density functions and introduce a significant amount of backscatter of energy from the subgrid to the resolved scales without causing numerical stability problems. The improvements in the SGS dissipation predictions in turn enhances the predicted resolved statistics such as the mean scalar, scalar fluxes, Reynolds stresses, and correlation lengths. Moreover, the nonalignment between the SGS stress and resolved strain-rate tensors predicted by the EASM with stochastic extension is in much closer agreement with direct numerical simulation data. © *2014 AIP Publishing LLC*. [http://dx.doi.org/10.1063/1.4879436]

I. INTRODUCTION

Marstorp *et al.*[1] presented the explicit algebraic subgrid-scale (SGS) model (EASM) for the SGS stresses in large eddy simulation (LES). Performance of the EASM, a nonlinear mixed model, has been demonstrated for the case of turbulent channel flow at various Reynolds numbers and grid resolutions, channel flow with system rotation in different directions and channel flow with periodic constrictions.[1–4] These studies illustrate the importance of the nonlinear SGS stress term in the EASM and showed that the assumption of an isotropic linear relationship between the SGS stress and resolved strain-rate tensor, as in the eddy-viscosity models, is not valid in wall-bounded turbulent flows where the SGS anisotropy is appreciable. The complementary explicit algebraic SGS scalar flux model (EASFM) proposed in Rasam, Brethouwer, and Johansson[3] is a nonlinear tensor eddy-diffusivity model which does not assume alignment between the SGS scalar flux and resolved scalar gradient vectors and provides a better physical representation of the SGS fluxes than the conventional eddy diffusivity model. It uses the SGS stress tensor in its formulation, consistent with the physics of the SGS scalar flux,[5] and naturally takes into account the effects of system rotation. It

[a]Electronic mail: rasam@mech.kth.se.

has been successfully applied to LES of channel flow with passive scalar transport with and without system rotation,[3] where it has been shown that the proper tensor eddy-diffusivity formulation of the EASFM improves LES predictions. Since the quality of scalar predictions is closely related to the velocity predictions,[3,6] it is natural to use the EASFM in combination with the EASM. The EASM and EASFM not only improve the predictions of the individual SGS stresses and scalar fluxes over the isotropic eddy-viscosity and eddy-diffusivity models, but also improve the characteristics of the SGS dissipation of energy[2,3] at a wide range of resolutions, as demonstrated by a SGS activity parameter analysis.[7]

Most SGS models are based on an equilibrium assumption between SGS production and dissipation and are often dissipative and deterministic functions of resolved quantities. By contrast, *a priori* studies of the energy transfer between the resolved and unresolved scales have revealed a strong intermittent nature[8] and a considerable amount of incoherent noise in the SGS.[9] In fact, filtered direct numerical simulation (DNS) data of channel flow shows that the forward- and backward-transfer of energy between the resolved and unresolved scales are almost equal in magnitude and both are much larger than the mean SGS dissipation.[10] The bidirectional nature of the energy transfer between the resolved and unresolved scales has also been found using the spectral closure theories such as the eddy-damped quasi-normal Markovian (EDQNM).[11]

In Leonard's decomposition of the SGS stresses,[12] the forward-scatter is caused by the interaction of the resolved velocities in the Leonard stresses which is often modeled using the eddy-viscosity concept. The backscatter is due to the interaction of unresolved and resolved velocities in the cross-stresses. Although the backscatter of energy is of physical importance to the dynamics of the wall-bounded flows,[10,11,13–16] there are only a few SGS models that can successfully account for that in LES. Simple Smagorinsky[17] and eddy-diffusivity type models with a constant coefficient do not predict the backscatter of energy since the SGS stresses and scalar fluxes are fully aligned with the strain-rate tensor and scalar-gradient vector, respectively. The dynamic procedure proposed by Germano *et al.*[18] for the Smagorinsky and eddy-diffusivity models[19] can predict backscatter of energy through a negative eddy viscosity and eddy diffusivity, but this causes numerical instabilities for realistic amounts of backscatter. Mixed models, which are based on a combination of the scale similarity model[20] and an eddy-viscosity or eddy-diffusivity model,[21–24] can in principle model backscatter of energy and a more intermittent SGS dissipation since the SGS stresses and scalar fluxes are less correlated with the strain-rate tensor and resolved scalar gradient, respectively. However, the amount of backscatter has to be controlled to prevent numerical instability.[25] The nonlinear SGS stress model by Kosovic[26] and the dynamic nonlinear SGS stress model by Wang and Bergstrom[27] can account for backscatter of energy caused by the non-alignment of the SGS stress and the resolved strain-rate tensors. The amount of backscatter in the Wang and Bergstrom[27] model in the case of turbulent channel flow can be up to 20% of the forward scatter. There have been a number of recent studies on the physical and scale space distribution of energy using the generalized balance equation of the second-order structure function for turbulent channel flow[28,29] showing that the backscatter of energy is related to the cyclic self-sustaining mechanisms of wall-turbulence. In this view, backscatter of energy is considered as a crucial element and should be accounted for by the SGS models.

One way to properly introduce randomness to the SGS stresses and scalar fluxes and get backscatter of energy is by implementing a stochastic process in the SGS model. Early LES models with stochastic extensions based on EDQNM were mostly suitable for simulations of homogeneous turbulence and not easily extendable to more complex flows.[30,31] Simpler stochastic models suitable for LES of wall-bounded flows have been proposed by, e.g., Leith,[32] Mason and Thompson,[33] Schumann.[34] Leith[32] used spatially and temporally uncorrelated random SGS stresses obtained from the rotation of a stochastic vector potential, with a variance estimated from dimensional reasoning, to include random SGS stresses in a Smagorinsky model. The stochastic process reproduced the k^4 slope of the backscatter spectrum in isotropic homogeneous turbulence.[35] It was found that the backscatter in LES of a two-dimensional shear mixing layer with this stochastic model was able to excite growth of resolved turbulent energy. The same approach was used by Mason and Thompson[33] to simulate boundary layer flows. The amount of backscatter was based on EDQNM predictions for an infinite inertial sub-range. Their model could remedy the over-prediction of the

mean velocity gradients by the Smagorinsky model close to the surface and gave more small-scale turbulence in accordance with experimental observations and a more correct shape of the probability density function (PDF) of energy transfer outside the viscous sublayer in channel flow.[36] Langevin stochastic differential equations (LSDE)[37] were used by Schumann[34] to construct isotropic random SGS stresses and scalar fluxes to extend Smagorinsky and eddy diffusivity models. The stochastic model was found essential for a proper prediction of the power law of the energy decay in isotropic turbulence. Carati, Ghosal, and Moin[38] extended a dynamic localization model with a stochastic term and observed improvements in the energy spectra in decaying turbulence. Wei *et al.*[39] used LSDE in LES of passive scalar dispersion with a hybrid Eulerian–Lagrangian method and found improvements in the two-time correlation as well as scalar dispersion. In Marstorp, Brethouwer, and Johansson,[40] LSDE was used to extend the Smagorinsky model. The model gave the proper k^4 scaling of the backscatter spectrum, enabled control of the length- and time scales of the SGS energy transfer, and improved the shape of the enstrophy spectrum at the smallest resolved scales and their time scales in isotropic turbulence. In LES of channel flow, this stochastic extension of the constant coefficient Smagorinsky model improved the variance and length scale of the dissipation as well as the mean streamwise velocity and Reynolds stresses. Zamansky, Vinkovic, and Gorokhovski[41] used a stochastic formulation in the form of a SGS acceleration appearing directly in the Navier–Stokes equations. The magnitude and orientation of the SGS acceleration were based on two separate stochastic processes. Turbulent channel flow simulations with this model in combination with the Smagorinsky model showed improvements in the spatial two-point correlations of velocity at moderate Reynolds numbers and resolutions, over the Smagorinsky model. Recently, Adams[42] extended the approximate deconvolution model using an Eulerian transformation of the generalized Langevin model and showed improvements in the dissipation rate evolution for the case of a Taylor–Green vortex.

The aforementioned studies made clear that the inclusion of a stochastic term in SGS models can give meaningful improvements of both resolved and SGS statistics in various flow cases. In a similar way in this study, we aim to further improve the EASM and EASFM by stochastic extensions of the SGS stresses and scalar fluxes using the approach proposed by Marstorp, Brethouwer, and Johansson.[40] It will be shown through LES of channel flow at $Re_\tau = 590$ with passive scalar transport that this stochastic extension improves LES predictions of the resolved velocity and scalar statistics. Stochastic extension of the SGS scalar fluxes in the EASFM improves the SGS dissipation of the scalar variance which plays a central role in the prediction of the small-scale mixing in LES of reactive flows.[43–45] Another area where the small-scale dynamics is important and the current stochastic modeling could enhance LES predictions is particle transport and multiphase flows where the importance of the small-scale dynamics has been pointed out in several papers.[46,47] Stochastic forcing has been proposed to enhance modeling of the SGS velocity for particle dispersion (e.g., pollutant dispersion) in turbulent flows[48,49] and stochastic modeling can also play a role in improving the SGS forcing on the particles. Finally, the current stochastic extension may act as a stochastic forcing to address the interface problem in hybrid LES–Reynolds averaged Navier–Stokes (RANS) simulations where a quick development of the small-scale turbulence from the RANS to the LES zone is essential.[50]

II. GOVERNING EQUATIONS OF LES

The governing equations for LES including a passive scalar, using the summation convention, read

$$\frac{\partial \widetilde{u}_i}{\partial t} + \widetilde{u}_j \frac{\partial \widetilde{u}_i}{\partial x_j} = -\frac{1}{\rho}\frac{\partial \widetilde{p}}{\partial x_i} + \nu \frac{\partial^2 \widetilde{u}_i}{\partial x_j^2} - \frac{\partial \tau_{ij}}{\partial x_j}, \quad \frac{\partial \widetilde{u}_i}{\partial x_i} = 0, \tag{1}$$

$$\frac{\partial \widetilde{\theta}}{\partial t} + \widetilde{u}_j \frac{\partial \widetilde{\theta}}{\partial x_j} = \frac{\nu}{\mathrm{Pr}} \frac{\partial^2 \widetilde{\theta}}{\partial x_i^2} - \frac{\partial q_i}{\partial x_i}, \tag{2}$$

where $\widetilde{\cdot}$ denotes a grid-filtered quantity, $\widetilde{u}_i$, $\widetilde{\theta}$, and $\widetilde{p}$ are the filtered velocity, passive scalar, and pressure, respectively, and Pr is the Prandtl number. The SGS stress tensor and scalar flux vector

are $\tau_{ij} = \widetilde{u_i u_j} - \widetilde{u}_i \widetilde{u}_j$ and $q_i = \widetilde{u_i \theta} - \widetilde{u}_i \widetilde{\theta}$, respectively, which have to be modeled to close the equations.

The effects of the SGS stresses and scalar fluxes on the resolved scales are best illustrated by the equations of the resolved kinetic energy $K = \widetilde{u}_i \widetilde{u}_i / 2$[51] and scalar intensity $K_\theta = \widetilde{\theta}\,\widetilde{\theta}/2$[6]

$$\underbrace{\frac{\partial K}{\partial t} + \frac{\partial}{\partial x_j}(\widetilde{u}_j K)}_{\text{advection}} = \underbrace{-\nu \frac{\partial \widetilde{u}_i}{\partial x_j}\frac{\partial \widetilde{u}_i}{\partial x_j}}_{\substack{\text{viscous}\\ \text{dissipation}}} \underbrace{- \frac{\partial}{\partial x_i}\left(\widetilde{u}_i \widetilde{p} + \nu \frac{\partial K}{\partial x_i} - \widetilde{u}_i \tau_{ij}\right)}_{\text{diffusion}} \underbrace{- (-\tau_{ij}\widetilde{S}_{ij})}_{\substack{\text{SGS}\\ \text{dissipation}}}, \tag{3}$$

$$\underbrace{\frac{\partial K_\theta}{\partial t} + \frac{\partial}{\partial x_j}(\widetilde{u}_j K_\theta)}_{\text{advection}} = \underbrace{-\frac{\nu}{\mathrm{Pr}} \frac{\partial \widetilde{\theta}}{\partial x_j}\frac{\partial \widetilde{\theta}}{\partial x_j}}_{\substack{\text{molecular}\\ \text{dissipation}}} \underbrace{- \frac{\nu}{\mathrm{Pr}} \frac{\partial^2 K_\theta}{\partial x_j \partial x_j} - \frac{\partial}{\partial x_j}(\widetilde{\theta} q_j)}_{\text{diffusion}} \underbrace{- (-q_j \frac{\partial \widetilde{\theta}}{\partial x_j})}_{\substack{\text{SGS}\\ \text{dissipation}}}. \tag{4}$$

The advection, viscous, and molecular dissipation and diffusion terms are denoted in the equations. The last terms on the right-hand sides represent the transfer of kinetic energy and scalar intensity from the resolved scales to SGS. The diffusion terms transfer energy in space but do not dissipate energy in a volume-averaged sense. The mean SGS dissipation terms are negative sink terms and dissipate energy. They also act as source terms in the corresponding equations of the SGS kinetic energy and scalar intensity. The instantaneous SGS dissipation can attain both positive and negative values meaning a transfer of energy to or from the subgrid-scales.

III. EXPLICIT ALGEBRAIC SGS STRESS MODEL

The EASM[1] is derived from the modeled transport equations of the SGS stress anisotropy and is inspired by the explicit algebraic model for the RANS equations.[52] The model is given by

$$\tau_{ij} = \frac{2}{3} K^{\mathrm{SGS}} \delta_{ij} + \beta_1 K^{\mathrm{SGS}} \widetilde{S}^*_{ij} + \beta_4 K^{\mathrm{SGS}} (\widetilde{S}^*_{ik}\widetilde{\Omega}^*_{kj} - \widetilde{\Omega}^*_{ik}\widetilde{S}^*_{kj}), \tag{5}$$

where δ_{ij} is the Kronecker delta, β_1 and β_4 are model coefficients, $K^{\mathrm{SGS}} = \tau_{kk}/2$ is the SGS kinetic energy and the normalized resolved strain- and rotation-rate tensors are defined as

$$\widetilde{S}^*_{ij} = \frac{\tau^*}{2}\left(\frac{\partial \widetilde{u}_i}{\partial x_j} + \frac{\partial \widetilde{u}_j}{\partial x_i}\right), \quad \widetilde{\Omega}^*_{ij} = \frac{\tau^*}{2}\left(\frac{\partial \widetilde{u}_i}{\partial x_j} - \frac{\partial \widetilde{u}_j}{\partial x_i}\right), \tag{6}$$

where $\tau^* = K^{\mathrm{SGS}}/\varepsilon$ (ε is the viscous dissipation of K^{SGS}) is the modeled time scale of the SGS motions.

The first term on the right-hand side of Eq. (5) is the isotropic part, the second term is an eddy-viscosity part, and the third term is a nonlinear tensor that models the anisotropy of the SGS stresses. Therefore, the EASM is a nonlinear mixed model. Since it ignores the quadratic terms of the resolved strain-rate tensor, which are responsible for the backscatter of energy,[26] it does not provide for backscatter. However, it has the nonlinear term including the products of the resolved strain- and rotation-rate tensors, which is responsible for the non-alignment of the SGS stress and resolved strain-rate tensors.[53]

The EASM employed here uses dynamic determination of K^{SGS} as[54]

$$K^{\mathrm{SGS}} = c\,\Delta^2 |\widetilde{S}_{ij}|^2, \tag{7}$$

where c is dynamically determined using the Germano identity with averaging in the homogeneous directions

$$c = \frac{1}{2}\frac{\widehat{\widetilde{u}_k \widetilde{u}_k} - \widehat{\widetilde{u}}_k \widehat{\widetilde{u}}_k}{\widehat{\Delta}^2 |\widehat{\widetilde{S}}_{ij}|^2 - \widehat{\Delta^2 |\widetilde{S}_{ij}|^2}}. \tag{8}$$

Here, $\Delta = \sqrt[3]{\Delta_x \Delta_y \Delta_z}$ is the grid filter size and $\widehat{\cdot}$ denotes test filtering with $\widehat{\Delta} = 2\,\Delta$. In this study, filtering is carried out using a sharp spectral filter in the homogeneous directions. The β_1 and β_4

coefficients in the EASM determine the relative contribution of the eddy-viscosity and the nonlinear terms, see Eq. (5), and are given by

$$\beta_4 = -\frac{6}{5}\left[(9c_1/4)^2 + |\widetilde{\Omega}^*_{ij}|^2\right]^{-1}, \quad \beta_1 = \frac{9}{4}c_1\beta_4, \tag{9}$$

where $|\widetilde{\Omega}^*_{ij}| = \sqrt{2\widetilde{\Omega}^*_{ij}\widetilde{\Omega}^*_{ij}}$ is the norm of the normalized resolved rotation-rate tensor.

A. Choice of the model parameters

In the derivation of the EASM, the Rotta's return to isotropy model is used for modeling the slow term of the model for the pressure strain-rate tensor[55] and the model parameter c_1 in Eq. (9) is the Rotta coefficient. This coefficient is adapted to wall-bounded flows according to Ref. 56 (in RANS) and is determined from the dynamic coefficient c (in LES) as

$$c_1 = c_1'\sqrt{c_3'}\frac{c^\alpha}{(2C_s)^{2.5}}, \quad c_1' = 2.13, \quad c_3' = 1.2, \quad C_s = 0.1, \quad \alpha = 1.1. \tag{10}$$

This means that β_1 and β_4 are influenced by the return to isotropy coefficient c_1. The factor 6/5 in Eq. (9) is due to the linear term in the model for the rapid part of the pressure strain-rate tensor. In Marstorp *et al.*[1] a factor 33/20 is used instead of 6/5 which makes the model slightly more dissipative, but the current choice allows for a less dissipative scheme, found to be more suitable for this stochastic extension, and is the same as the corresponding value in the explicit algebraic RANS model. Hence, the stochastic extension allows us to go back to the original RANS value which is found from the rapid distortion theory. The value of α in Eq. (10) is also lower than 1.25 proposed in the original model.[1] This change does not affect the velocity predictions but the original value was found to cause a discontinuity in the near-wall prediction of the wall-normal SGS scalar flux in the EASFM and therefore was lowered to alleviate the problem. This value for α has been used with the EASFM and EASM in Rasam, Brethouwer, and Johansson[3] for LES of channel flow with and without system rotation with scalar transport at different resolutions and Prandtl numbers. The SGS time scale, τ^*, is modeled by

$$\tau^* = c_3'\frac{1.5C_k^{1.5}\sqrt{c}}{2C_s}|\widetilde{S}_{ij}|^{-1}. \tag{11}$$

Due to the change in the coefficient from 33/20 to 6/5 in Eq. (9) we use different values for c_1' and c_3' in Eq. (10).[57] The coefficient $C_k = 1.5$ is the Kolmogorov constant, see Marstorp *et al.*[1] for details.

The EASM and EASFM have been successfully applied for LES of different flows. The good performance of these models for LESs of channel flow with and without system rotation at different Reynolds numbers and resolutions shows a good degree of universality of the model coefficients.[1–3] The EASM has also been used for LES of channel flow with streamwise periodic hill-shaped constrictions at different resolutions using a second-order finite volume Navier–Stokes solver,[4] where good LES predictions have been obtained. The changes in the model coefficients proposed in this study for the EASM improve the model performance with the stochastic extension and are within the range that are found from *a priori* evaluations in Marstorp *et al.*[1] In this study, the grid filter is a spectral cutoff due to the spectral discretization. The good performance of the EASM for different discretization schemes with spectral and box filters have been verified in Rasam[4] showing the independence of the model coefficients on the type of the grid filter.

IV. EXPLICIT ALGEBRAIC SGS SCALAR FLUX MODEL

The EASFM[3] is a nonlinear mixed tensor eddy diffusivity model based on the explicit algebraic scalar flux model for the RANS equations.[58] It is expressed as

$$q_i = -(1 - c_{4\theta})\tau^* A_{ij}^{-1}\tau_{jk}\frac{\partial\widetilde{\theta}}{\partial x_k}, \tag{12}$$

where the time scale, τ^*, is the SGS time scale computed from Eq. (11). The matrix A_{ij} is a linear function of the normalized strain- and rotation rate tensors $A_{ij} = c_{1\theta}\delta_{ij} + c_s\widetilde{S}^*_{ij} + c_\Omega\widetilde{\Omega}^*_{ij}$ and its inverse is found from the Cayley–Hamilton theorem

$$\mathbf{A^{-1}} = \frac{(c_{1\theta}^2 - \frac{1}{2}Q_1)\mathbf{I} - c_{1\theta}(c_S\widetilde{\mathbf{S}}^* + c_\Omega\widetilde{\Omega}^*) + (c_S\widetilde{\mathbf{S}}^* + c_\Omega\widetilde{\Omega}^*)^2}{c_{1\theta}(c_{1\theta}^2 - \frac{1}{2}Q_1) + \frac{1}{2}Q_2}, \tag{13}$$

where boldface notation indicates tensors, $\mathbf{I}$ is the identity matrix, $c_s = 0.2$ and $c_\Omega = 0.5$ are model constants. Q_1 and Q_2 are functions of the invariants of the normalized strain- and rotation-rate tensors

$$Q_1 = c_s^2 tr(\widetilde{\mathbf{S}}^{*2}) + c_\Omega^2 tr(\widetilde{\Omega}^{*2}), \quad Q_2 = \frac{2}{3}c_s^3 tr(\widetilde{\mathbf{S}}^{*3}) + 2c_s c_\Omega^2 tr(\widetilde{\mathbf{S}}^*\widetilde{\Omega}^{*2}). \tag{14}$$

The model coefficient $c_{1\theta}$ is given as

$$c_{1\theta} = c'_{1\theta}\left(\mathrm{Pr}\,|\widetilde{\mathrm{S}}^*_{\mathrm{ij}}|\right)^{0.7}\frac{K^{\mathrm{SGS}}}{0.1\Delta|\widetilde{S}_{ij}|}, \quad c'_{1\theta} = 0.2, \tag{15}$$

and its lower limit is set to 0.5. In order to take into account the filter size dependence and improve $c_{1\theta}$ predictions at test-filter level, a correction to $c'_{1\theta}$ in the form

$$c'_{1\theta}(2\Delta) = 10^{-x}\,c'_{1\theta}(\Delta), \quad x = 0.1\left(Re_{2\Delta}^{0.7} - Re_{\Delta}^{0.7}\right) - 0.3, \quad Re_{n\Delta} = (n\Delta)^2|\widetilde{S}_{ij}|/\nu, \tag{16}$$

is applied where $Re_{n\Delta}$ is the mesh Reynolds number. Similar to the c_1 coefficient in the EASM, the $c_{1\theta}$ coefficient is due to the modeling of the slow part of the pressure-scalar gradient vector in the transport equation for the SGS scalar fluxes and is based on the Rotta's return to isotropy concept adapted to LES. The model coefficient $c_{4\theta}$ is computed dynamically using the Germano identity for the SGS scalar flux.[3] In the computations, $1 - c_{4\theta}$ is limited to positive values for stability of the simulations, implying that backscatter is prohibited. No spatial averaging is necessary to smooth out the dynamic coefficient.

V. LANGEVIN STOCHASTIC DIFFERENTIAL EQUATION

The stochastic extension of the Smagorinsky and eddy diffusivity models proposed by Marstorp, Brethouwer, and Johansson[40] uses the solution to the LSDE[37] to introduce stochastic fluctuations to the instantaneous SGS stresses and scalar fluxes. The LSDE of the stochastic process $\mathscr{X}(x,t)$ reads

$$d\mathscr{X}(x,t) = -a\mathscr{X}(x,t)dt + b\sqrt{2a}\;d\mathscr{W}(x,t), \tag{17}$$

where a and b are constants. The first term on the right-hand side is a drift term and the second term is a random number with $\mathscr{W}(x,t)$ as the Wiener process which generates spatially and temporally uncorrelated random numbers with zero mean and unit variance. The solution to (17) is a stationary process with zero mean and b^2 variance.[4] The relaxation time-scale of the process, $\tau_{\mathscr{X}}$, is inversely proportional to a, i.e., $\tau_{\mathscr{X}} = 1/a$. A more familiar form of the stochastic process can be obtained by discretizing Eq. (17)

$$\mathscr{X}(x,t+\Delta t) = (1 - \frac{\Delta t}{\tau_{\mathscr{X}}})\mathscr{X}(x,t) + b\sqrt{2\frac{\Delta t}{\tau_{\mathscr{X}}}}\;d\mathscr{W}(x,t), \tag{18}$$

where Δt is the time step of the simulations. Similar to Heinz[59] we model τ_X, using dimensional analysis, as

$$\tau_{\mathscr{X}} = C_{\mathscr{X}}\frac{\Delta}{\sqrt{K^{\mathrm{SGS}}}}, \tag{19}$$

where $C_{\mathscr{X}} = 0.05$ is a model constant obtained from *a posteriori* analysis of LES in channel flows. If model (7) is used for K^{SGS}, $\tau_{\mathscr{X}}$ is found as

$$\tau_{\mathscr{X}} = \frac{C_{\mathscr{X}}}{\sqrt{c}|\widetilde{S}_{ij}|}, \tag{20}$$

where c is the dynamic coefficient, see Eq. (7).

VI. STOCHASTIC EXPLICIT ALGEBRAIC MODELS

Following Marstorp, Brethouwer, and Johansson,[40] we extend the eddy-viscosity part of the EASM with a stochastic process $\mathscr{X}_1$ as

$$\tau_{ij} = \frac{2}{3}K^{SGS}\delta_{ij} + (1 + \mathscr{X}_1(x,t))\,\beta_1 K^{SGS}\widetilde{S}^*_{ij} + \beta_4 K^{SGS}(\widetilde{S}^*_{ik}\widetilde{\Omega}^*_{kj} - \widetilde{\Omega}^*_{ik}\widetilde{S}^*_{kj}). \tag{21}$$

The second term on the right-hand side contributes to the SGS dissipation but the first and last terms do not. The last term influences the geometrical relation between the strain-rate and SGS stress tensors. In essence, including a stochastic process gives rise to backscatter of energy by allowing negative values for the eddy viscosity.

Similar to the EASM, a stochastic extension of the EASFM is obtained as

$$q_i = -(1 - c_{4\theta})\tau^* A^{-1}_{ij}\tau_{jk}\frac{\partial\widetilde{\theta}}{\partial x_k}\,(1 + \mathscr{X}_2(x,t))\,. \tag{22}$$

The stochastic processes $\mathscr{X}_1$ and $\mathscr{X}_2$ are governed by the LSDE in Eq. (18) with the time scales $\tau_{\mathscr{X}1}$ according to Eq. (20) and $\tau_{\mathscr{X}2} = \mathrm{Pr}\,\tau_{\mathscr{X}1}$ following the relation[60] $\tau_\theta = \mathrm{Pr}\,\tau^*$, where τ_θ and τ^* are the time scales of the SGS scalar and velocity fields, respectively. Variances of $\mathscr{X}_1$ and $\mathscr{X}_2$ are determined by b_1 and b_2. The values $b_1 = 1.4$ and $b_2 = 1.2$ are chosen such that a good agreement for the variance of the SGS dissipation between the DNS and LES is obtained. Slight changes in the b_1 and b_2 coefficients do not significantly change the LES predictions. However, a significant increase in these coefficients leads to larger amounts of backscatter of energy which leads to numerical instabilities.

VII. SIMULATIONS

To test the stochastic explicit algebraic models, LESs of channel flow are carried out using a pseudo-spectral Navier–Stokes solver with Fourier representation in wall-parallel directions (x and z) and Chebyshev representation in the wall-normal direction (y), using the Chebyshev–tau method. Aliasing errors are removed using the 3/2-rule.[61] The time integration is carried out with a four-step third-order Runge–Kutta scheme for the nonlinear terms and a second-order Crank–Nicolson scheme for the linear terms.[62] A passive scalar field (temperature) is included in the simulations. The walls are kept at constant and uniform but different temperatures and a no-slip condition is applied for the velocity at the walls.

LESs are carried out using a constant mass flux constraint with a bulk Reynolds number $Re_b = u_b h/\nu = 10\,935$. Specifications of the simulations are given in Table I. Results are compared to the DNS at[3] $Re_\tau = u_\tau h/\nu = 590$, which is essentially the same as the DNS of Moser, Kim, and Mansour,[63] and also includes a scalar (temperature) with $\mathrm{Pr} = 0.71$. The LES domain size ($L_x = 2\pi h, L_z = \pi h$, h is the channel half-width) and bulk Reynolds number are the same as those of the reference DNS. In order to compare LES and DNS results of the SGS quantities, DNS velocity and

TABLE I. Summary of numerical simulations. Δ_x^+, Δ_z^+, and Δ_y^+ are streamwise, spanwise, and wall-normal resolutions in wall-units in physical space, respectively. A stochastic (S) or non-stochastic (N) SGS stress model is indicated by the first letter of the case name (S or N) and the corresponding stochastic (S) or non-stochastic (N) SGS scalar flux model is indicated by the second letter of the case name (S or N). The stochastic extensions of the EASM and EASFM are denoted by SEASM and SEASFM.

Case	b_1	b_2	Re_τ	Δ_x^+	Δ_z^+	Δ_y^+ min ∼ max	Nusselt number	Subgrid-scale model Stress	Subgrid-scale model Scalar flux
N–N	0	0	592	58.1	29.0	0.71–28.9	8.53	EASM	EASFM
S–N	1.4	0	589	57.8	28.8	0.70–28.7	8.69	SEASM	EASFM
S–S	1.4	1.2	589	57.8	28.8	0.70–28.7	8.70	SEASM	SEASFM
DNS	...	...	587	9.6	4.8	0.04–7.2	8.76	...	...

scalar fields are filtered to the LES resolution using a sharp cut-off filter in Fourier space in the homogeneous directions.

VIII. EFFECTS OF THE STOCHASTIC EXTENSION ON LES OF CHANNEL FLOW

In this section, we first investigate the effects of stochastic extension on the resolved statistics of the velocity and scalar and then demonstrate the effects on the modeled SGS dissipation statistics and the relative alignment of the SGS stresses and resolved strain-rate tensors. We analyze three LES cases. Case N–N uses non-stochastic (N) SGS models for SGS stresses and scalar fluxes, case S–N uses a stochastic (S) SGS stress model and a non-stochastic (N) SGS scalar flux model, and case S–S uses stochastic (S) models for both SGS stresses and scalar fluxes. Cases S–N and S–S are hence equivalent for the velocity statistics.

A. Mean velocity and Reynolds stresses

The mean streamwise velocity profiles for cases N–N and S–N are shown in Figures 1(a) and 1(b). The LES results both agree well with the DNS data but closer observation shows that case S–N is more accurate than case N–N, especially in the logarithmic layer ($50 < y^+ < 200$, see Figure 1(b)) where the stochastic extension produces a better equilibrium between the production and dissipation of kinetic energy. Inclusion of the stochastic term also slightly affects the wall shear due to the generation of more small-scale turbulence in the buffer layer, see the Re_τ predictions in Table I which are very close to the DNS value.

The Reynolds stresses (i.e., sum of the resolved and SGS stresses) predicted by case N–N and S–N are both in good agreement with the DNS as well and the impact of the stochastic term on the Reynolds stresses is small, see Figures 1(c) and 1(d). However, a shift in the peak of the streamwise Reynolds stress R^+_{uu} toward the wall and a reduction of R^+_{uu} in the buffer layer is observed indicating a reduction in the length scale of the near-wall structures due to the stochastic extension, see Figure 1(d). The location and magnitude of the peak of R^+_{uu} matches the DNS data well in case S–N with the stochastic extension. A small improvement in the peak value of the spanwise and wall-normal components in the buffer layer and a small over-prediction of the spanwise component of the Reynolds stresses in the outer layer can also be observed while the shear stress remains almost the same. These findings show that although predictions of case N–N are close to the DNS data, the stochastic modeling in case S–N is able to further improve the Reynolds stresses and mean velocity profiles.

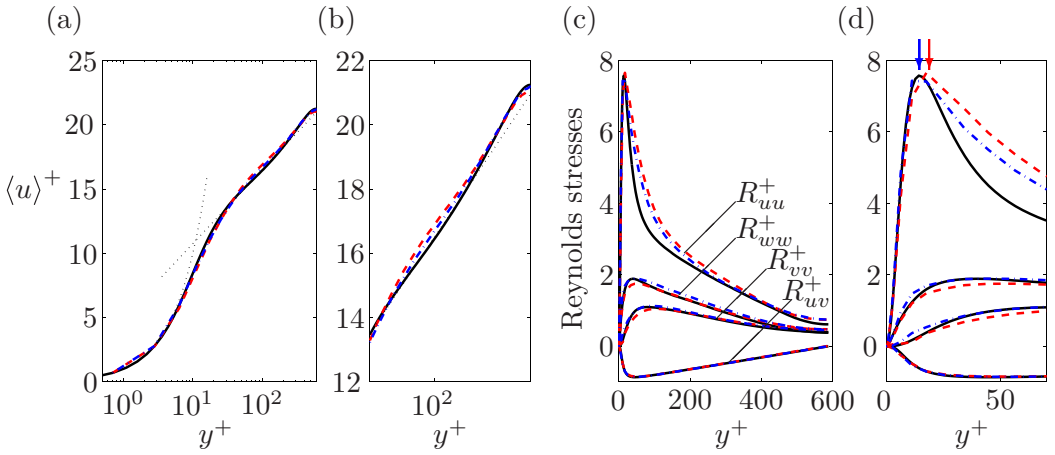

FIG. 1. Mean velocity profiles (a) and the closeup of its logarithmic region (b); resolved plus modeled streamwise (R^+_{uu}), spanwise (R^+_{ww}), wall-normal (R^+_{vv}), and shear (R^+_{uv}) Reynolds stresses in wall units (c) and the closeup of its near-wall region (d); Arrows point to the location of the maximum of R^+_{uu}. _____ : DNS, ___ . ___ : case S–N, and ___ ___ : Case N–N.

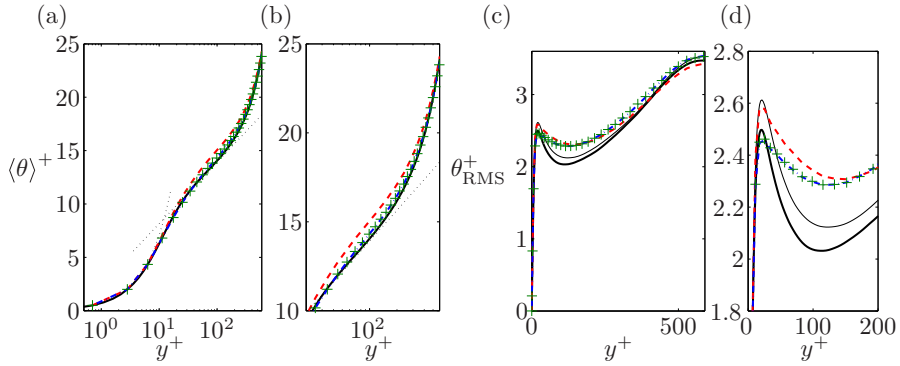

FIG. 2. Mean scalar profiles (a) and the closeup of its logarithmic region (b); root-mean-square (RMS) of the scalar fluctuations (c) and the closeup of its buffer and outer layer (d); ▬ : filtered DNS, ___ : DNS, _ . _ : case S–N, _ _ : case N–N, and + : case S–S.

B. Mean and root-mean-square (RMS) of scalar and scalar fluxes

Performance of the SGS scalar flux model depends on the SGS stress model,[3,6] since the scalar field depends on the predicted velocity field. This is also true for the EASFM which directly includes the SGS stresses in its formulation, see Eq. (12). Therefore, we expect that the improvements in the velocity predictions in case S–N influence LES predictions even when no stochastic term is implemented in the SGS scalar flux model. The mean scalar profiles from cases N–N, S–N, and S–S are shown in Figures 2(a) and 2(b). Predictions of case S–N indeed show an appreciable improvement in the mean scalar profile, especially in the logarithmic layer, and practically coincide with the DNS data, see Figure 2(b).

Turbulent Prandtl number defined as

$$Pr_t = \frac{\langle u'v'\rangle / (\partial\langle u\rangle/\partial y)}{\langle v'\theta'\rangle / (\partial\langle\theta\rangle/\partial y)} \tag{23}$$

is the ratio of the apparent diffusivity of momentum to that of heat.[64] Close observation of the mean scalar profiles shows that they are shallower in the buffer layer and the beginning of the logarithmic layer in case S–N and S–S than in case N–N, implying a higher molecular dissipation, a decrease in the turbulent Prandtl number and therefore an increase in the diffusivity of the scalar, which could also be observed in case of the SGS Prandtl number, as noted by Schumann.[34] One can also observe an important improvement in the Nusselt number predictions, see Table I, due to a higher heat transfer. The stochastic extension of the SGS stress model promotes finer turbulent structures in the buffer layer, as will be shown later, which apparently enhances mixing near the wall. Predictions of case S–S do not show further improvements in the mean scalar profile compared to case S–N as was also observed by Mason and Thompson.[33] However, the S–N predictions practically coincide with the DNS data so there is no room for further improvements to be expected in case S–S.

Predictions of the resolved RMS of the scalar fluctuations, θ^+_{rms}, show improvements in the magnitude of the near-wall peak in case S–N compared to case N–N. Case N–N over-predicts the near-wall peak whereas the S–N prediction of the near-wall peak matches the filtered DNS data well, see Figures 2(c) and 2(d). The near-wall peak of θ^+_{rms} corresponds to the peak in the scalar intensity production and is affected by the SGS dissipation. Therefore, the better prediction of the peak value in case S–N is likely caused by the influence of the stochastic extension on the SGS dissipation dynamics.

Predictions of scalar fluxes $\langle v'\theta'\rangle$ and $\langle v'\theta'\rangle$ are shown in Figures 3(a)–3(d). Case S-N shows a better prediction of the peak value of $\langle v'\theta'\rangle$ than case N–N, see Figures 3(a) and 3(b). Improvements in the near-wall prediction of $\langle v'\theta'\rangle$ in case S–N compared to case N–N are observed and the results practically coincide with the DNS data. Inclusion of a stochastic term in the SGS scalar flux model does not lead to further improvements in the $\langle v'\theta'\rangle$ and $\langle v'\theta'\rangle$ predictions.

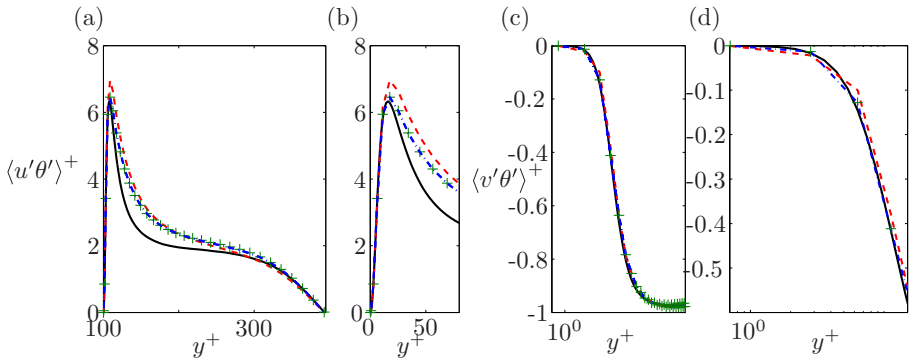

FIG. 3. Resolved plus modeled streamwise scalar flux, $\langle u'\theta'\rangle^+$ (a) and the closeup of its near-wall region (b), in wall units; resolved plus modeled wall-normal scalar flux, $\langle v'\theta'\rangle^+$ (c) and the closeup of its near-wall region (d), in wall units; ___ : DNS, _ . _ : case S–N, _ _ : case N–N, and + : case S–S.

C. Two-point correlations of the velocity and the integral length scales

We analyze the length scales in the streamwise direction via two-point correlations of the velocity fluctuations defined as

$$B^x_{u_iu_i}(y,r) = \frac{\langle \widetilde{u}_i'(x,y,z)\widetilde{u}_i'(x+r,y,z)\rangle}{\langle \widetilde{u}_i'^2(x,y,z)\rangle},\ i=1,2,3,\ \text{(no summation over i)}, \tag{24}$$

where r is the separation distance and $\widetilde{u}_i'$ are the resolved velocity fluctuations. The two-point correlation for the scalar fluctuations is computed in the same way. The corresponding integral length-scales are

$$\mathscr{L}_x[\widetilde{u}_i] = \int_0^{\frac{1}{2}L_x} \frac{\langle \widetilde{u}_i'(x,y,z)\widetilde{u}_i'(x+r,y,z)\rangle}{\langle \widetilde{u}_i'(x,y,z)^2\rangle} dx. \tag{25}$$

Here, $\langle . \rangle$ denotes averaging both in time and in the spanwise direction. The streamwise two-point correlations of the velocity components and scalar fluctuations using Eq. (24) are presented in Figures 4(a)–4(d) at a near-wall location, $y^+ \approx 5$ together with the DNS data. The plots are accompanied by the corresponding integral length scale plots using Eq. (25) to show the variation across the channel. The velocity correlations in case S–N show appreciable improvements compared to case N–N near the wall, with the largest improvement observed for the streamwise velocity. However, the integral length-scale plot also shows that case S–N predicts a shorter correlation length than case N–N and the DNS for $y^+ > 80$, see Figure 4(a). Close observation reveals that the DNS and case N–N predictions of B^x_{uu} do not go to zero in the logarithmic layer due to the insufficient length of the box, while in case S–N it does. This shows that the stochastic part effectively reduces the size of the eddies in the streamwise direction. We also observe that B^x_{vv} at $y^+ \approx 5$ and $\mathscr{L}_x[\widetilde{v}]$ in case S–N agree better with DNS than the results of case N–N, see Figure 4(c). For B^x_{ww}, cases S–N and N–N have similar predictions as the DNS results and the predicted length scales are nearly the same in the two cases across the channel.

Contrary to the velocity correlations, only marginal improvements are observed for the scalar correlations $B^x_{\theta\theta}$. This could mean that the time scale of the stochastic events is not long enough to influence the relevant large scales and further affect the correlation lengths for the scalar. However, the relative error in the scalar predictions are close to that of the velocity in case S–N, see Figures 4(a) and 4(b).

The LES predictions of spanwise two-point velocity correlations depend on how well the near-wall turbulent structures are resolved close to the wall.[65] A good representation of those correlations can be achieved by resolving these structures with fine spanwise resolution and one should expect deviations at coarse resolutions,[2,66] see Sec. VIII D. The near-wall turbulent structures are indeed too large compared to the DNS, but all the statistics are reasonably predicted implying that the near-

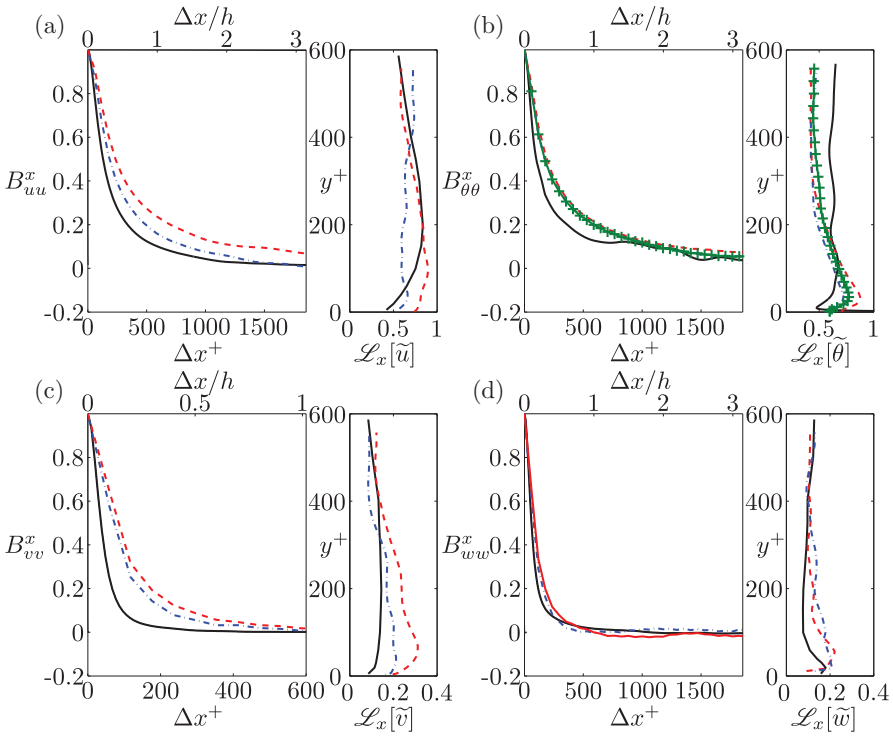

FIG. 4. Streamwise two-point correlation functions of the scalar (b) and the streamwise (a), wall-normal (c) and spanwise (d) velocities plotted at a wall distance of $y^+ \approx 5.0$. The corresponding length scales computed from the two-point correlation functions at all wall distances accompany each plot. ——— : DNS, — . — : case S–N, — — : case N–N, and — + — : case S–S.

wall cycle is correctly represented. The stochastic formulation has a small effect on the spanwise correlations, results are not shown for brevity but similar results are reported in Rasam *et al.*[2] for the EASM predictions at a higher Reynolds number, where LES predictions show wider streak spacings in the spanwise direction compared to the DNS data.

D. Premultiplied spanwise spectra of the streamwise velocity

More extensive information on the effect of the stochastic term on the turbulent structures can be deduced from one-dimensional premultiplied spectra of the streamwise velocity in the spanwise direction, see Figures 5(a)–5(d). The DNS spectrum (not presented) has a peak in the buffer layer at $y^+ \approx 15$ and length scale $\lambda_z^+ \approx 120$, marked by the crosses in Figures 5(a) and 5(b), corresponding to the spacing of near-wall streaks.[67] Cases N–N and S–N predict the wall-distance of the near-wall peak quite accurate but they over-predict its length scale λ_z^+, which indicates that the LES predicts much wider streaks, see Figures 5(a) and 5(b). However, the spanwise resolution in the LES is quite coarse and this puts a lower limit on the streak spacing even when a stochastic term is used.

The spectra also have a peak in the outer layer at $y/h \approx 0.35$ corresponding to the large-scale structures which have a characteristic size of O(h), see Figures 5(c) and 5(d). The corresponding peak in the DNS spectrum is marked by the crosses in Figures 5(c) and 5(d). The location of this peak is reasonably well predicted in cases S–N and N–N. However, the length-scale of this peak in case S–N is in better agreement with the DNS data. This shows that the stochastic term not only affects the small scales but also the largest turbulent scales, possibly as a result of the backscatter of energy induced by the stochastic model, see Sec. VIII E. A further study on the premultiplied spectra for the EASM can be found in Rasam *et al.*[2] at a higher Reynolds number.

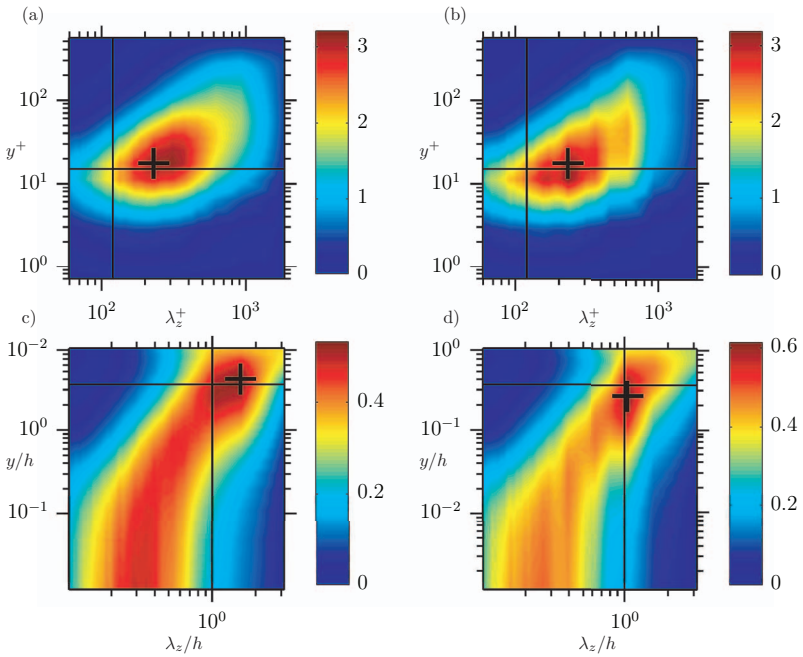

FIG. 5. Premultiplied spanwise spectrum of the streamwise velocity as a function of the spanwise wavelength λ_z^+ and wall distance y^+ presented in inner units $k_z E_{uu}^{1D}/u_\tau^2$ (a) and (b) and in outer units $k_z E_{uu}^{1D}/u_{\text{rms}}^2$ as a function of λ_z and y/h (c) and (d). Figures (a) and (c) are from case N–N; figures (b) and (d) are from case S–N. Crosses indicate the peaks of energy of the LES and lines indicate the corresponding peaks for the DNS.

E. Mean and RMS of SGS dissipation and forward and backscatter of energy

One of the goals of the stochastic extension of the SGS models is to improve the SGS dissipation. We define the SGS dissipation for the kinetic energy as in (3) and for the scalar variance as in (4). For the SEASM and SEASFM, these become

$$\Pi = \frac{\beta_1}{2\tau^*} K^{\text{SGS}} |\widetilde{S}_{ij}^*|^2 (1 + \mathscr{X}), \quad \chi = -(1 - c_{4\theta}) A_{ij}^{-1} \tau_{jk} \frac{\partial \widetilde{\theta}}{\partial x_k} \frac{\partial \widetilde{\theta}}{\partial x_i} (1 + \mathscr{X}), \tag{26}$$

where it can be seen that the stochastic process directly induces variations in the SGS dissipation. Energy transfer by the SGS dissipation can be further split into

$$\Pi = \Pi^+ + \Pi^- \quad \text{and} \quad \chi = \chi^+ + \chi^-, \tag{27}$$

where Π^+ and χ^+ are the forward scatter and Π^- and χ^- are the backscatter of kinetic energy and scalar variance, respectively. Statistics of the SGS dissipation for all cases are shown in Figures 6(a)–6(d). It is interesting to observe that the statistics of the SGS dissipation of the scalar variance differ from those of the kinetic energy. While the mean and RMS of the SGS dissipation approach zero at the center of the channel for the kinetic energy, those of the scalar variance stay finite. This is due to the fact that the production of the turbulent kinetic energy is zero in the middle of the channel, but the production of the scalar variance is not. Cases N–N and S–N both predict a correct forward scatter $\langle \Pi^+ \rangle$, see Figure 6(a), but the S–N prediction of the location of the peak is more accurate. Their prediction of the mean SGS dissipation, $\langle \Pi \rangle$, is higher than the corresponding DNS value. The stochastic extension induces backscatter of energy and reduces the peak of $\langle \Pi \rangle$ by 15%, see Figure 6(c). Despite this over-prediction of $\langle \Pi \rangle$, the cases predict the mean velocity and Reynolds stresses in good agreement with the DNS as shown in Figures 1(a)–1(d).

Cases N–N and S–N under-predict $\langle \chi^+ \rangle$, while case S–S improves its predictions, especially its peak value, see Figure 6(a). Cases S–N and S–S slightly improve the magnitude and location of

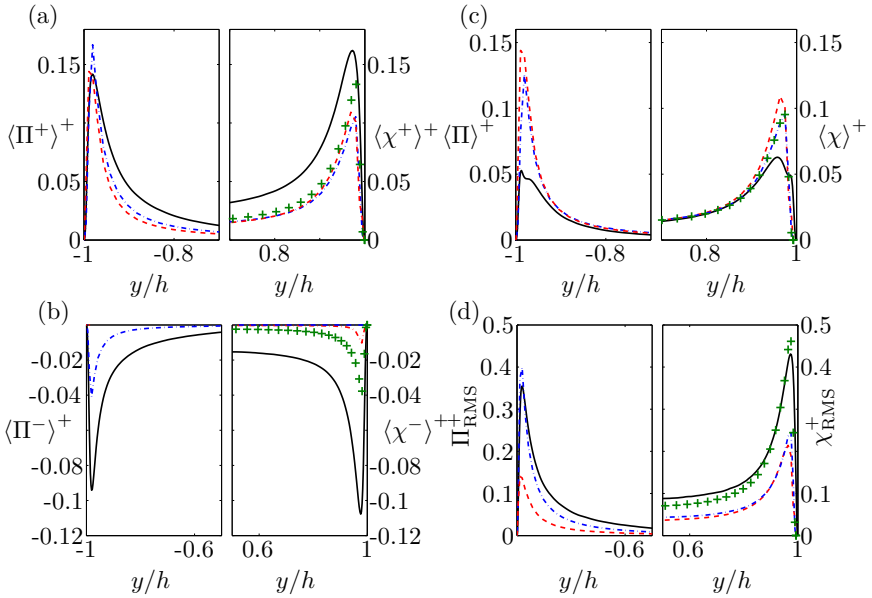

FIG. 6. (a) Forward scatter, (b) backscatter, and (c) total SGS dissipation and (d) root-mean-square (RMS) of the total SGS dissipation in wall units. ——— : DNS data, — . — : case S–N, — — : case N–N, and + : case S–S. Note that the left half of each figure shows the statistics of the SGS dissipation of kinetic energy and the right half of each figure shows the corresponding statistics of the SGS dissipation of the scalar variance.

the peak of $\langle\chi\rangle$ in comparison with case N–N. Case S–S provides a backscatter whose peak value is up to 40% of that of the DNS, while case N–N does not give any backscatter, see Figure 6(b). It is interesting to note that case S–N gives rise to backscatter in the scalar predictions, but its value is small (around 10% in the peak value) compared to the actual value computed from the filtered DNS data.

Subgrid-scale stresses predicted by scale similarity models are known to have high correlations with the real SGS stresses and give backscatter of energy. We have tried a mixed scale similarity model,[24] where the scale similarity model is combined with a dynamic eddy viscosity model. This model was tested for the channel flow simulations presented in this paper and it was found that the backscatter of the kinetic energy provided by the stochastic EASM is comparable to the prediction of this mixed scale similarity model. However, comparable predictions of other resolved statistics with the EASM and DNS data were not given by this model. Hence, these results are not presented here.

The introduction of stochastic terms lead to a more intermittent SGS dissipation and higher RMS values and indeed there are considerable improvements in the RMS of the SGS dissipation for both Π and χ using stochastic extensions, showing a very good agreement with the DNS data, see Figure 6(d).

F. Length-scale of the SGS dissipation

Another improvement that was achieved by the stochastic extension of the explicit algebraic SGS models is the length-scale of the SGS dissipation, $\mathscr{L}_x[\Pi]$ and $\mathscr{L}_x[\chi]$. It is a measure of intermittency and is computed from the spatial two-point correlation of its fluctuating part.[40] For Π, it is expressed as

$$\mathscr{L}_x[\Pi] = \int_0^{\frac{1}{2}L_x} \frac{\langle \Pi'(x,y,z)\Pi'(x+r,y,z)\rangle}{\langle \Pi'^2(x,y,z)\rangle} dx,$$

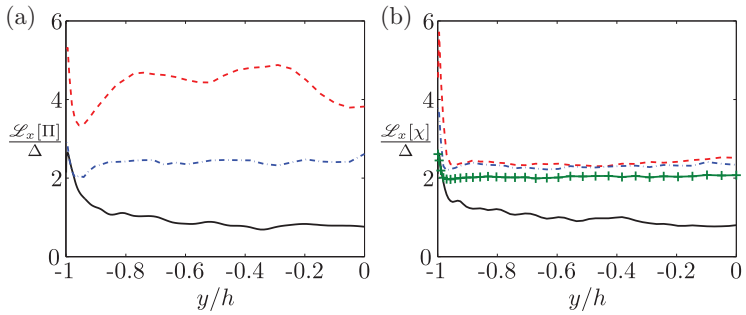

FIG. 7. Length scale of the SGS kinetic energy (a) and scalar variance dissipation (b) normalized with the grid-sale $\Delta = \sqrt[3]{\Delta_x \langle \Delta_y \rangle \Delta_z}$. ——— : DNS, ——.—— : case S–N, —— —— : case N–N, and ——+—— : case S–S.

where Π' is the fluctuating part of Π and $\langle . \rangle$ denotes both time and spatial averaging in the spanwise direction. A similar expression can be written for χ. The SGS dissipation length scales computed from Eq. (28) are shown in Figures 7(a) and 7(b), where they have been normalized by the grid-filter scale $\Delta = \sqrt[3]{\Delta_x \langle \Delta_y \rangle \Delta_z}$. Here, $\langle \Delta_y \rangle$ denotes the mean grid spacing in the wall-normal direction. The SGS dissipation length-scale computed from the filtered DNS data is slightly smaller than Δ, see also Marstorp, Brethouwer, and Johansson,[40] which signifies the presence of a large amount of spatially uncorrelated variations in the SGS dissipation. Predictions in case N–N are almost four times larger than Δ in most of the channel and even larger close to the wall. In case S–N, the predicted length scale is about two times Δ in the core of the channel, in better agreement with the DNS, and close to the DNS data near the wall, see Figure 7(a). The coarse resolution presumably puts a lower limit on this length scale.

Predictions of $\mathscr{L}_x[\chi]$ in case N–N are closer to the DNS data than $\mathscr{L}_x[\Pi]$, see Figure 7(b). This is due to the direct influence of the dynamic procedure in the computations of the EASFM, which introduces more variations in the SGS fluxes and therefore the SGS dissipation. One can also see from Figure 6(d) that the peak value of χ^+_{RMS} predicted by case N–N is 56% of that of the DNS, while the corresponding value for Π^+_{RMS} in case N–N is 43%. The stochastic term does not reduce $\mathscr{L}_x[\chi]$ in the core of the channel, but improves it close to the wall. In case S–S, the length-scale in the whole channel is in better agreement with the DNS and matches the DNS data close to the wall. Its predictions are about two times Δ. These results show that the length-scales are reduced and the SGS dissipation becomes more intermittent by introducing stochastic models.

G. Anisotropy of the SGS dissipation

An important property of the SGS dissipation tensor is its anisotropy defined as[68]

$$I_{22} = \frac{\left\langle \left(\tau_{22}\widetilde{S}_{22}\right)^2 \right\rangle}{\left\langle \left(\tau_{11}\widetilde{S}_{11}\right)^2 \right\rangle}. \tag{28}$$

In Marstorp *et al.*,[1] it was shown that the EASM improves the anisotropy of the SGS dissipation over the dynamic Smagorinsky model. Here, we find that case S–N predicts a larger SGS dissipation anisotropy I_{22} in the core of the channel, closer to the filtered DNS data than case N–N, see Figure 8.

H. Probability density functions of the SGS dissipation

Further statistical information on the influence of the stochastic extension on the SGS dissipation can be obtained by analyzing its PDF, see Figures 9(a)–9(f). PDFs are plotted at different locations

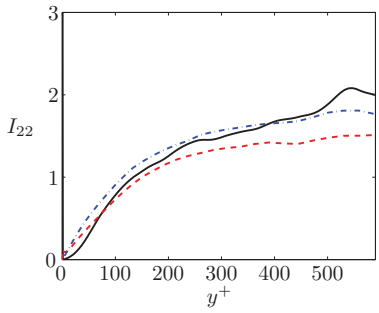

FIG. 8. Anisotropy of the SGS dissipation, I_{22}. _____ : DNS, __ __ : case N–N, and __ . __ : case S–N.

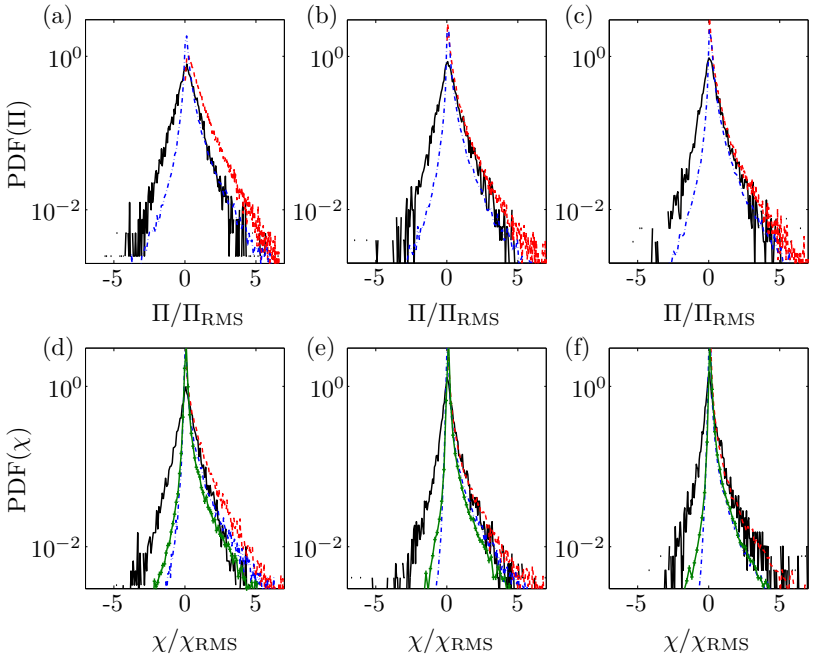

FIG. 9. Probability density functions (PDFs) of subgrid-scale dissipation at (a) and (d) $y^+ \approx 15$, (b) and (e) $y^+ \approx 50$, and (c) and (f) $y^+ \approx 100$; _____ : DNS, __ . __ : case S–N, __ __ : case N-N, and __ + __ : case S–S. Plots are scaled to unit area. (a)–(c) are for the kinetic energy dissipation and (d)–(f) are for the scalar intensity dissipation.

from the wall and are scaled to unit area. The distances are chosen at $y^+ \approx 15$, close to the location of the peak of the SGS dissipation, $y^+ \approx 50$ located close to the beginning of the logarithmic region, and at $y^+ \approx 100$, in the middle of the logarithmic region. In general, the PDF of the filtered DNS data is slightly skewed toward positive values but the negative tail is more prominent than the positive one ensuring a negative mean dissipation, i.e., a mean energy transfer from the resolved to the subgrid-scales. At all wall distances case S–N clearly predicts more accurate forward energy transfer than case N–N for Π and it also provides for a reasonable backscatter. Especially at $y^+ \approx 15$ near the peak of the SGS dissipation the improvements are appreciable. The highly intermittent behavior of Π in the turbulent channel flow where the amount of back- and forward scatter are of similar magnitude, makes it difficult for any SGS model to give satisfactory predictions. Nevertheless, the improvements obtained in case S–N are significant.

The same trend is observed in case S–S compared to case N–N concerning the scalar variance energy transfer, see Figures 9(d)–9(f). It is observed that in case S–N some backscatter of energy

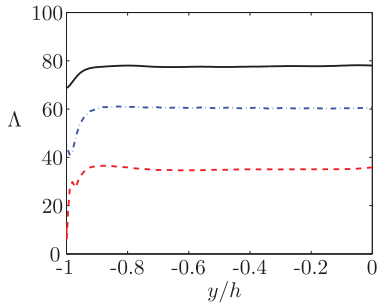

FIG. 10. Mean angle between the eigenvectors of $\widetilde{S}_{ij}$ and $-\tau_{ij}$, corresponding to the largest eigenvalues. ——— : filtered DNS, — — : case N–N, and — . — : case S–N.

due to the randomness in the SGS stresses is predicted but it is small. In case S–S, there are more backscatter events than in case S–N.

I. Tensorial alignment of the SGS stress tensor

The tensorial alignment between the SGS stress and strain-rate tensors in *a priori* studies of DNS data as well as SGS model predictions have been examined by Marstorp *et al.*,[1] Wang and Bergstrom,[27] Horiuti,[53] Borue and Orszag,[69] Tao, Katz, and Meneveau.[70,71] We follow the approach by Wang and Bergstrom[27] and Marstorp *et al.*[1] and calculate the averaged angles $\Lambda \in [0^\circ, 90^\circ]$ between the eigenvectors corresponding to the most negative eigenvalues of $-\tau_{ij}$ and $\widetilde{S}_{ij}$. The filtered DNS data show a mean angle of around 80° in a large part of the channel. Eddy-viscosity SGS stress models predict $\Lambda = 0^\circ$ since they have an isotropic formulation. The EASM is an anisotropic SGS stress model, so that τ_{ij} is not aligned with $\widetilde{S}_{ij}$. In fact, a mean angle of almost 40° is predicted in case N–N, see Figure 10, which is a large improvement compared to the dynamic Smagorinsky model. In case S–N, the relative alignment of the predicted SGS stresses and the resolved strain-rate tensor is further reduced from 40° to 60°, see Figure 10.

IX. MODEL PERFORMANCE AT OTHER RESOLUTIONS

We have assessed the performance of the stochastic explicit algebraic models at resolutions other than the one presented earlier for LES of channel flow at $Re_\tau = 590$. In this section, the prediction of the mean velocity, streamwise Reynolds stress, mean and RMS of temperature as well as the PDFs of the SGS dissipation at $y^+ \approx 15$ are discussed for a coarser and a finer resolution, see Table II. For brevity, results for the combination of the EASFM and SEASM are not presented and only results of the SEASFM with the SEASM are presented. The results have been found to be insensitive to the resolution.

TABLE II. Summary of numerical simulations. See Table I for more information.

Case	b_1	b_2	Re_τ	Δ_x^+	Δ_z^+	Δ_y^+ min ∼ max	Nusselt number	Subgrid-scale model Stress	Subgrid-scale model Scalar flux
N–1	0	0	586	38.0	19.0	0.31–19.2	8.63	EASM	EASFM
N–2	0	0	593	77.6	38.8	0.71–29.0	8.66	EASM	EASFM
S–1	1.4	1.2	587	38.5	19.3	0.31–19.2	8.81	SEASM	SEASFM
S–2	1.4	1.2	581	76.0	38.0	0.72–29.0	8.77	SEASM	SEASFM

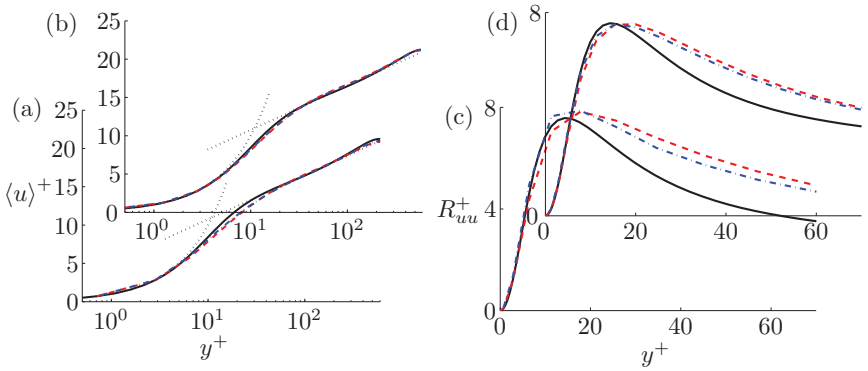

FIG. 11. Mean velocity profiles for the coarse (a) and fine (b) grids in wall units. Resolved plus modeled streamwise Reynolds stress (R^+_{uu}) for the coarse (c) and fine (d) grids in wall units. ——— : DNS; — . — : cases S–1 and S–2; — — : Cases N–1 and N–2.

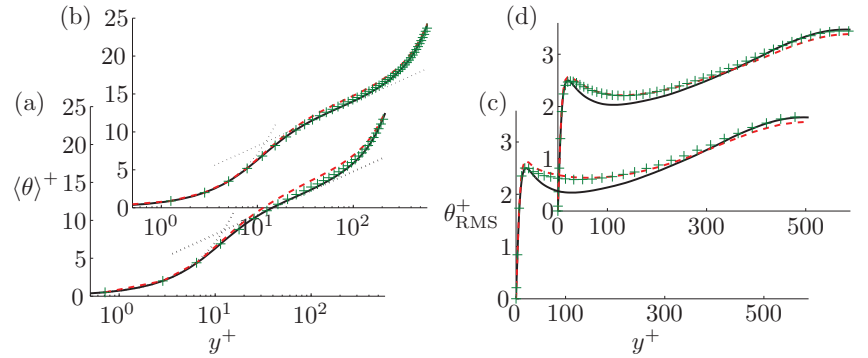

FIG. 12. Mean temperature profiles for the coarse (a) and fine (b) grids. Root-mean-square (RMS) of the temperature in wall units for the coarse (c) and fine (d) grids. ——— : DNS; — + — : cases S–1 and S–2; — — : Cases N–1 and N–2.

The mean velocity profiles are shown in Figures 11(a) and 11(b). The N–1 and N–2 predictions are in excellent agreement with the DNS data and the improvements due to the stochastic extension in cases S–1 and S–2 are marginal. The streamwise Reynolds stress predictions show the same improvements as was observed earlier in case S–S. The predictions converge to the DNS with increasing resolution.

The temperature predictions are shown in Figures 12(a) and 12(b). There is an appreciable improvement in the mean temperature profiles in the logarithmic region in case S–2 compared to case N–2, while the differences are less between cases N–1 and S–1. The RMS profiles of the temperature show improvements in the peak values in case S–2 compared to case N–2, see Figure 12(c), but at the fine resolution model predictions are similar.

The PDFs of the SGS dissipation are shown in Figures 13(a)–13(d) for $y^+ \approx 15$, in the buffer layer. With the stochastic extension, the PDFs of the SGS dissipation for the kinetic energy Π are in much better agreement with the DNS data for the forward scatter events, i.e., positive tails of the PDFs. The stochastic extension also gives an appreciable energy backscatter in cases S–1 and S–2, see Figures 13(a) and 13(b). These observations hold for both resolutions. The stochastic extension also introduces a fare amount of backscatter of scalar energy at both resolutions as shown by the PDFs of the SGS dissipation of scalar intensity χ. It improves the forward scatter of scalar energy at the fine resolution but not at the coarse resolution, see Figures 13(c) and 13(d). All in all, these results confirm the conclusions that the anisotropy-resolving character of these SGS models give a

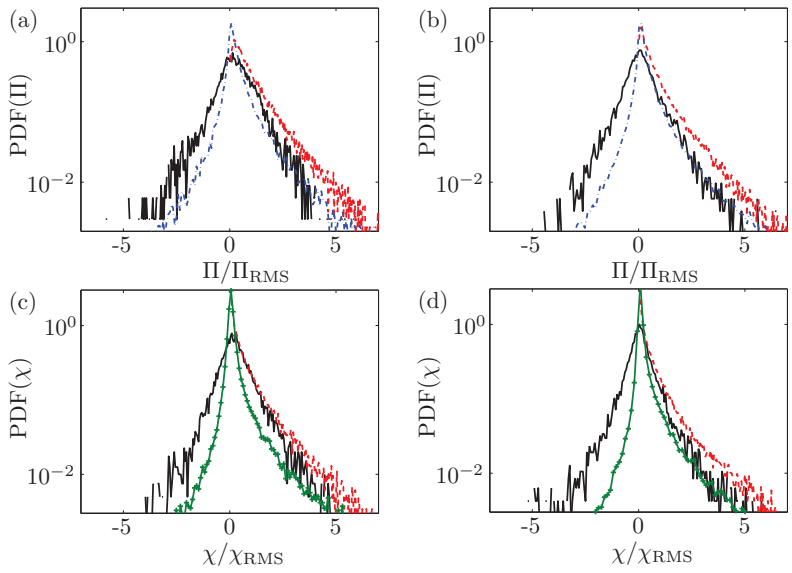

FIG. 13. Probability density functions (PDFs) of the SGS dissipation for the kinetic energy Π at $y^+ \approx 15$ for the coarse (a) and fine (b) grids. ——— : DNS data; ——.—— : PDF(Π) for cases S–1 and S–2; —— —— : PDF(Π) for cases N–1 and N–2. PDFs of the SGS dissipation for the scalar intensity χ at $y^+ \approx 15$ for the coarse (c) and fine (d) grids. ——— : DNS data; —— + —— : PDF(χ) for cases S–1 and S–2; —— —— : PDF(χ) for cases N–1 and N–2.

high degree of insensitivity to grid resolution, and that the stochastic extensions give some significant improvements.

X. CONCLUSIONS

LES of turbulent channel flow including a passive scalar at $Re_\tau = 590$ was carried out to investigate the stochastic extensions of the explicit algebraic SGS stress and scalar flux models.[1,3] This study shows that, although the resolved quantities are well predicted by the non-stochastic models, inclusion of the stochastic process further improves the velocity related statistics, such as the mean velocity and Reynolds stresses. These improvements also lead to better predictions of the passive scalar statistics, such as the mean and fluxes of the scalar. The predicted streamwise two-point correlations of velocity as well as the corresponding integral length scales are in closer agreement with the DNS data with the stochastic extension. The models with the stochastic extensions also provide for a reasonable amount of backscatter of turbulent kinetic energy and scalar variance and a larger intermittency of the SGS dissipation, in better agreement with DNS data. Finally, the stochastic extension of the SGS models improved the geometrical representation of the SGS stress tensor by reducing its alignment with the resolved strain-rate tensor. Application of the stochastic explicit algebraic models at different resolutions showed that the improvements observed in this study persist at a relatively wide range of resolutions.

The better representation of the SGS quantities achieved by the stochastic extensions is essential for a number of applications where small-scale processes play a crucial role in LES. A few examples are LES of turbulent combustion where the SGS dissipation plays an important role in the prediction of the small-scale mixing, LES of sprays, advection of particles in turbulent flows, and other interesting multiphase applications where the SGS forces due to the SGS stresses are important in the dynamics of the particles or the droplets. The stochastic extension of the explicit algebraic SGS models presented here could contribute to a better prediction of the SGS mixing or forces in these cases. This can be a subject for further investigations. A further application of the current stochastic extension is in hybrid LES–RANS simulations where generation of the small-scale turbulence at the LES–RANS interface is essential.

ACKNOWLEDGMENTS

Support from the Swedish research council through Grant No. 621-2010-6965 and computer time provided by the Swedish National Infrastructure for Computing (SNIC) are gratefully acknowledged.

[1] L. Marstorp, G. Brethouwer, O. Grundestam, and A. V. Johansson, "Explicit algebraic subgrid stress models with application to rotating channel flow," J. Fluid. Mech. **639**, 403–432 (2009).
[2] A. Rasam, G. Brethouwer, P. Schatter, Q. Li, and A. V. Johansson, "Effects of modelling, resolution and anisotropy of the subgrid-scales on large eddy simulations of channel flow," J. Turbul. **12**, 1–20 (2011).
[3] A. Rasam, G. Brethouwer, and A. V. Johansson, "An explicit algebraic model for the subgrid-scale passive scalar flux," J. Fluid Mech. **721**, 541–577 (2013).
[4] A. Rasam, "Anisotropy-resolving subgrid-scale modelling using explicit algebraic closures for large eddy simulation," Ph.D. thesis, KTH Royal Institute of Technology, 2014.
[5] S. Chumakov, "*A priori* study of subgrid-scale flux of a passive scalar homogeneous turbulence," Phys. Rev. E **78**, 1–11 (2008).
[6] C. Jiménez, L. Valino, and C. Dopazo, "*A priori* and *a posteriori* tests of subgrid scale models for scalar transport," Phys. Fluids **13**, 2433 (2001).
[7] B. J. Guerts and J. Fröhlich, "A framework for predicting accuracy limitations in large-eddy simulation," Phys. Fluids **14**, L41–L44 (2002).
[8] S. Cerutti and C. Meneveau, "Intermittency and relative scaling of subgrid-scale energy dissipation in isotropic turbulence," Phys. Fluids **10**, 928 (1998).
[9] G. Destefano, D. E. Goldstein, and O. V. Vasilyev, "On the role of subgrid-scale coherent modes in large-eddy simulation," J. Fluid Mech. **525**, 263–274 (2005).
[10] U. Piomelli, W. Cabot, P. Moin, and S. Lee, "Subgrid-scale backscatter in turbulent and transitional flows," Phys. Fluids A **3**, 1766 (1991).
[11] D. C. Leslie and G. Quarini, "The application of turbulence theory to the formulation of subgrid modeling procedures," J. Fluid Mech. **91**, 65–91 (1979).
[12] A. Leonard, "Energy cascade in large-eddy simulations of turbulent fluid flows," Adv. Geophys. A **18**, 237–248 (1975).
[13] C. Härtel, L. Kleiser, F. Unger, and R. Friedrich, "Subgrid-scale energy transfer in the near-wall region of turbulent flows," Phys. Fluids **6**, 3130–3143 (1994).
[14] J. A. Domardzaki, W. Liu, and M. E. Brachet, "An analysis of subgrid scale interactions in numerically simulated isotropic turbulence," Phys. Fluids A **5**, 1747–1759 (1993).
[15] J. A. Domardzaki, W. Liu, C. Hartel, and L. Kleiser, "Energy transfer in numerically simulated wall-bounded flows," Phys. Fluids **6**, 1583–1599 (1994).
[16] D. Dunn and J. Morrison, "Anisotropy and energy flux in wall turbulence," J. Fluid Mech. **491**, 353–378 (2003).
[17] J. Smagorinsky, "General circulation experiments with the primitive equations. I. The basic experiment," Mon. Weather Rev. **91**, 99–164 (1963).
[18] M. Germano, U. Piomelli, P. Moin, and W. Cabot, "A dynamic subgrid-scale eddy viscosity model," Phys. Fluids A **3**, 1760–1765 (1991).
[19] P. Moin, K. Squires, W. Cabot, and S. Lee, "A dynamic subgrid-scale model for compressible turbulence and scalar transport," Phys. Fluids A **3**, 2746 (1991).
[20] J. Bardina, J. H. Freziger, and W. C. Reynolds, "Improved subgrid-scale models for large eddy simulation," AIAA Paper No. 80-1357, 1980.
[21] Y. Zang, R. L. Street, and J. R. Koseff, "A dynamic mixed subgrid-scale model and its application to turbulent recirculating flows," Phys. Fluids A **5**, 3186 (1993).
[22] M. Salvetti and S. Banerjee, "*A priori* tests of a new dynamic subgrid-scale model for finite-difference large-eddy simulations," Phys. Fluids **7**, 2831 (1995).
[23] K. Horiuti, "A new dynamic two-parameter mixed model for large-eddy simulation," Phys. Fluids **9**, 3443 (1997).
[24] R. Akhavan, A. Ansari, S. Kang, and N. Mangiavacchi, "Subgrid-scale interactions in a numerically simulated planar turbulent jet and implications for modelling," J. Fluid Mech. **408**, 83–120 (2000).
[25] S. Liu, C. Meneveau, and J. Katz, "On the properties of similarity subgrid-scale models as deduced from measurements in a turbulent jet," J. Fluid Mech. **275**, 83–119 (1994).
[26] B. Kosovic, "Subgrid-scale modelling for the large-eddy simulation of high-Reynolds-number boundary layers," J. Fluid Mech. **336**, 151–182 (1997).
[27] B. Wang and D. Bergstrom, "A dynamic nonlinear subgrid-scale stress model," Phys. Fluids **17**, 1–15 (2005).
[28] A. Cimarelli and E. De Angelis, "Anisotropic dynamics and sub-grid energy transfer in wall-turbulence," Phys. Fluids **24**, 015102 (2012).
[29] A. Cimarelli, E. De Angelis, and C. Casciola, "Paths of energy in turbulent channel flows," J. Fluid Mech. **715**, 436–451 (2013).
[30] J. P. Bertoglio, "A stochastic grid model for sheared turbulence," *Macroscopic Modeling of Turbulent Flows* (Springer, Berlin, 1985), pp. 100–119.
[31] J. R. Chasnov, "Simulation of the Kolmogorov inertial subrange using an improved subgrid moodel," Phys. Fluids A **3**, 188–200 (1991).
[32] C. E. Leith, "Stochastic backscatter in a subgrid-scale model: Plane shear mixing layer," Phys. Fluids A **2**, 297–299 (1990).
[33] P. J. Mason and D. J. Thompson, "Stochastic backscatter in large-eddy simulations of boundary layers," J. Fluid Mech. **242**, 51–78 (1992).

[34] U. Schumann, "Stochastic backscatter of turbulence energy and scalar variance by random subgrid-scale fluxes," Proc. R. Soc. London, Ser. A **451**, 293–318 (1995).
[35] R. H. Kraichnan, "Eddy viscosity in two and three dimensions," J. Atmos. Sci. **33**, 1521–1536 (1976).
[36] P. S. Westbury, D. C. Dunn, and J. F. Morrison, "Analysis of a stochastic backscatter model for large-eddy simulation of all-bounded flow," Eur. J. Mech. B **23**, 738–758 (2004).
[37] P. Langevin, "Sur la theorie du mouvement brownien," C. R. Acad. Sci. **146**, 530–533 (1908).
[38] D. Carati, S. Ghosal, and P. Moin, "On the representation of backscatter in dynamic localization models," Phys. Fluids **7**, 606 (1995).
[39] G. Wei, I. Vinkovic, L. Shao, and S. Simoëns, "Scalar dispersion by a large-eddy simulation and a Lagrangian stochastic subgrid model," Phys. Fluids **18**, 095101 (2006).
[40] L. Marstorp, G. Brethouwer, and A. V. Johansson, "A stochastic subgrid model with application to turbulent flow and scalar mixing," Phys. Fluids **19**, 035107 (2007).
[41] R. Zamansky, I. Vinkovic, and M. Gorokhovski, "LES approach coupled with stochastic forcing of subgrid acceleration in a high-Reynolds-number channel flow," J. Turbul. **11**, 1–18 (2010).
[42] N. A. Adams, "A stochastic extension of the approximate deconvolution model," Phys. Fluids **23**, 055103 (2011).
[43] H. Pitsch, "Large-eddy simulation of turbulent combustion," Annu. Rev. Fluid Mech. **38**, 453–482 (2006).
[44] H. Pitsch and S. Fedotov, "Stochastic modeling of scalar dissipation rate fluctuations in non-premixed turbulent combustion," Center for Turbulence Research, Annual Research Briefs, 2000, Vol. 91.
[45] Z. Pouransari, L. Vervisch, and A. V. Johansson, "Heat release effects on mixing scales of non-premixed turbulent wall-jets: A direct numerical simulation study," Int. J. Heat Fluid Flow **40**, 65–80 (2013).
[46] F. Bianco, S. Chibbaro, C. Marchioli, M. Salvetti, and A. Soldati, "Intrinsic filtering errors of Lagrangian particle tracking in LES flow fields," Phys. Fluids **24**, 045103 (2012).
[47] W. Jones, S. Lyra, and A. Marquis, "Large eddy simulation of evaporating kerosene and acetone sprays," Int. J. Heat Mass Transfer **53**, 2491–2505 (2010).
[48] B. Geurts and J. Kuerten, "Ideal stochastic forcing for the motion of particles in large-eddy simulation extracted from direct numerical simulation of turbulent channel flow," Phys. Fluids **24**, 081702 (2012).
[49] B. Shotorban and F. Mashayek, "A stochastic model for particle motion in large-eddy simulation," J. Turbul. **7**, 1–16 (2006).
[50] J. Fröhlich and D. von Terzi, "Hybrid LES/RANS methods for the simulation of turbulent flows," Prog. Aerosp. Sci. **44**, 349–377 (2008).
[51] P. Sagaut, *Large Eddy Simulation for Incompressible Flows: An Introduction*, 3rd ed. (Springer, Berlin, Germany, 2010).
[52] S. Wallin and A. V. Johansson, "An explicit algebraic Reynolds stress model for incompressible and compressible turbulent flows," J. Fluid Mech. **403**, 89–132 (2000).
[53] K. Horiuti, "Roles of non-aligned eigenvectors of strain-rate and subgrid-scale stress tensors in turbulence generation," J. Fluid Mech. **491**, 65–100 (2003).
[54] A. Yoshizawa, "Statistical theory for compressible turbulent shear flows, with the application to subgrid modeling," Phys. Fluids **29**, 2152 (1986).
[55] S. B. Pope, *Turbulent Flows* (Cambridge University Press, New York, 2000).
[56] T. Sjögren and A. V. Johansson, "Development and calibration of algebraic nonlinear models for terms in the Reynolds stress transport equations," Phys. Fluids **12**, 1554 (2000).
[57] An error was found in the values given in Marstorp *et al.*[1] for these coefficients. $c_1' = 4.2$ and $c_3' = 2.4$ were given in the paper while the correct values are $c_1' = 3.12$ and $c_3' = 0.91$ which are also in better agreement with the *a priori* calculations.
[58] P. Wikström, S. Wallin, and A. V. Johansson, "Derivation and investigation of a new explicit algebraic model for passive scalar flux," Phys. Fluids **12**, 688–702 (2000).
[59] S. Heinz, "Realizability of dynamic subgrid-scale stress models via stochastic analysis," Monte Carlo Methods Appl. **14**, 311–329 (2008).
[60] C. Jiménez, F. Ducros, B. Cuenot, and B. Bédat, "Subgrid scale variance and dissipation of a scalar field in large eddy simulations," Phys. Fluids **13**, 1748 (2001).
[61] C. Canuto, M. Y. Hussaini, A. Quarteroni, and T. A. Zang, *Spectral Methods in Fluid Dynamics* (Springer-Verlag, 1988).
[62] M. Chevalier, P. Schlatter, A. Lundbladh, and D. S. Henningson, "Simson: A pseudo-spectral solver for incompressible boundary layer flows," Trita-MEK 2007:07 (KTH, Linné Flow Center, Stockholm, Sweden, 2007).
[63] R. D. Moser, J. Kim, and N. N. Mansour, "Direct numerical simulation of turbulent channel flow up to $Re_\tau = 590$," Phys. Fluids **11**, 943–945 (1999).
[64] P. Bradshaw and G. P. Huang, "The law of the wall in turbulent flow," Proc. R. Soc. London, Ser. A **451**, 165–188 (1995).
[65] A. G. Kravchenko, P. Moin, and R. D. Moser, "Zonal embedded grids for numerical simulations of wall-bounded turbulent flows," Comput. Phys. **127**, 412–423 (1996).
[66] U. Piomelli, "High Reynolds number calculations using the dynamic subgrid-scale stress model," Phys. Fluids A **5**, 1484–1490 (1993).
[67] J. C. Del Alamo, J. Jiménez, P. Zandonade, and R. D. Moser, "Scaling of the energy spectra of turbulent channels," J. Fluid Mech. **500**, 135–144 (2004).
[68] H. S. Kang and C. Meneveau, "Passive scalar anisotropy in a heated turbulent wake, new observations and implication for large eddy simulations," J. Fluid Mech. **442**, 161–170 (2001).
[69] V. Borue and S. A. Orszag, "Local energy flux and subgrid-scale statistics in three-dimensional turbulence," J. Fluid Mech. **366**, 1–31 (1998).
[70] B. Tao, J. Katz, and C. Meneveau, "Geometry and scale relationships in high Reynolds number turbulence determined from three-dimensional holographic velocimetry," Phys. Fluids **12**, 941–944 (2000).
[71] B. Tao, J. Katz, and C. Meneveau, "Statistical geometry of subgrid-scale stresses determined from holographic particle image velocimetry measurements," J. Fluid Mech. **457**, 35–78 (2002).